Differences in the Hydrological Cycle and Sensitivity Between Multiscale Modeling Frameworks with and without a Higher-order Turbulence Closure

Kuan-Man Xu [1], Zhujun Li[2], Anning Cheng [3], Peter N. Blossey[4], and Cristiana Stan[5]

[1] Climate Science Branch, NASA Langley Research Center, Hampton, VA.

[2] NASA Postdoctoral Program, University Space Research Association, Hampton, VA.

[3] Environmental Modeling Center, NOAA Center for Weather and Climate Prediction, College Park, MD.

[4] Department of Atmospheric Sciences, University of Washington, Seattle, WA.

[5] Department of Atmospheric, Oceanic and Earth Sciences, George Mason University, Fairfax, VA.

Corresponding author: Dr. Kuan-Man Xu

Email: Kuan-Man.Xu@nasa.gov

Key Points:

- SPCAM-IPHOC simulates higher global hydrological sensitivity for the slow response but lower sensitivity for the fast response than SPCAM
- The higher sensitivity is due to the higher sensitivity of surface sensible and latent heat fluxes and radiative cooling to surface warming
- The higher-order turbulence closure greatly impacts the hydrological sensitivity and sensible heat flux response over the tropical lands

Abstract

Current conventional global climate models (GCMs) produce a weak increase in global mean precipitation with anthropogenic warming in comparison with the lower-tropospheric moisture increases. The motive of this study is to understand the differences in the hydrological sensitivity between two multiscale modeling frameworks (MMFs) that arise from the different treatments of turbulence and low clouds in order to aid to the understanding of the model spread among conventional GCMs. We compare the hydrological sensitivity and its energetic constraint from MMFs with (SPCAM-IPHOC) or without (SPCAM) an advanced higher-order turbulence closure. SPCAM-IPHOC simulates higher global hydrological sensitivity for the slow response but lower sensitivity for the fast response than SPCAM. Their differences are comparable to the spreads of conventional GCMs. The higher sensitivity in SPCAM-IPHOC is associated with the higher ratio of the changes in latent heating to those in net atmospheric radiative cooling, which is further related to a stronger decrease in the Bowen ratio with warming than in SPCAM. The higher sensitivity of cloud radiative cooling resulting from the lack of low clouds in SPCAM is another major factor in contributing to the lower precipitation sensitivity. The two MMFs differ greatly in the hydrological sensitivity over the tropical lands, where the simulated sensitivity of surface sensible heat fluxes to surface warming and CO_2 increase in SPCAM-IPHOC is weaker than in SPCAM. The difference in divergences of dry static energy flux simulated by the two MMFs also contributes to the difference in land precipitation sensitivity between the two models.

1 Introduction

Current global climate models (GCMs) produce a weak increase (2.52±0.22% K^{-1}) in global mean precipitation with anthropogenic warming (hereafter, referred to as "hydrological sensitivity," or HS) in comparison with the lower-tropospheric moisture increase (6.5 to 7% K^{-1}) [e.g., *Allan et al*., 2014; *Andrews et al*., 2010; *Fläschner et al*., 2016; *Oueslati et al*., 2016]. The low HS relative to the moisture availability simulated by GCMs can be understood to arise from an energetic constraint [e.g., *Newell et al.*, 1975; *Mitchell et al.*, 1987; *Stephens and Ellis,* 2008; *O'Gorman et al*., 2012; *Allan et al.*, 2014]: a balance over a multi-year period of net atmospheric radiative cooling [i.e., longwave cooling (LWC) minus heating from shortwave absorption (SWA); signs of both LWC and SWA are positive], latent heating from precipitation (LP) and sensible heating from the surface (SH; positive for upward SH), where L is the latent heat of vaporization. That is,

$$LWC = LP + SWA + SH. \qquad (1),$$

Uncertainty in simulated HS is thus related to that in LWC, SWA and SH. For example, *DeAngelis et al.* [2015] recently attributed the spread in the simulated temperature-mediated SWA response to CO_2 forcing to differing sensitivities of solar absorption to atmospheric moisture [precipitable water (PW)] and related this to the HS spread among GCMs. They further suggested that improved representations of SWA by water vapor in radiative transfer parameterizations could reduce the uncertainty in the hydrological response. *Mauritsen and Stevens* [2015] attributed the muted precipitation response to the lack of the iris effect in GCMs, which increases longwave radiative cooling as the clearsky area expands with surface warming. *Stephens and Ellis* [2008] identified that the ratio of precipitation sensitivity to water vapor sensitivity is primarily determined by the clearsky radiative energy loss, with counteracting feedbacks from cloud radiative heating and reduction in surface sensible heating.

Radiative feedbacks associated with changes in temperature, water vapor, clouds and surface albedo, which are the major climate sensitivity components, can impact HS through their effect on the atmospheric energy budget, in addition to non-radiative feedback due to surface sensible heat flux changes [e.g., *Stephens and Ellis*, 2008; *Previdi*, 2000; *O'Gorman et al.*, 2012]. A large part of the uncertainty in climate sensitivity is attributed to that in cloud feedback, in particular, low clouds [e.g., *Vial et al.*, 2013], which explains a significant proportion of the intermodel HS spread, in addition to the surface sensible flux feedback, although they are smaller contributors to HS compared to water vapor and lapse rate feedbacks [e.g., *Previdi*, 2000].

The uncertainties in cloud and surface sensible heat flux feedbacks are related to representations of turbulence, cloud and precipitation processes in GCMs, the uncertainties of which can influence the precipitation efficiency and the HS spread in GCMs [*Stephens and Ellis*, 2008; *Previdi*, 2000; *Mauritsen and Stevens*, 2015]. The complexity of subgrid effects associated with clouds, convection, precipitation and radiation is the primary obstacle to improving model physical parameterizations in conventional GCMs [*Randall et al*., 2003]. The multiscale modeling framework (MMF) proposed by *Grabowski* [2001] and *Khairoutdinov and Randall* [2001] is an attractive tool because it explicitly simulates the largest and most organized circulations within deep convective systems using a cloud-system resolving model (CRM) within each grid column of the global model.

MMF has been used to perform climate change simulations with specified sea surface temperature (SST) perturbations [*Wyant et al*., 2006, 2012; *Bretherton et al*., 2014; *Xu and Cheng*, 2016] and fully coupled ocean [*Arnold et al*., 2014; *Stan and Xu*, 2014; *Bretherton et al*., 2014]. Using fixed SST experiments with warming of 2 K or 4 K, it is found that MMF simulates comparable or weaker climate sensitivity than most conventional GCMs, depending on the complexity of the turbulence scheme used by CRMs [*Wyant et al*. 2006; *Bretherton et al*. 2014; *Xu and Cheng*, 2016]. The effective climate sensitivity (ECS) is respectively 1.5 K in *Wyant et al.* [2006], 2.1 K in *Bretherton et al.* [2014] and 2.0 K in *Xu and Cheng* [2016] assuming a CO_2 doubling forcing of 3.7 W m^{-2} [*Myhre et al., 1998*], compared to 2.1-3.0 K for AMIP_4K (Atmospheric Model Intercomparison Project +4 K SST) simulations by conventional GCMs [*Ringer et al.*, 2014]. The simulations analyzed by *Wyant et al*. [2006] and *Bretherton et al*. [2014] were produced using a low-order turbulence closure whereas simulations analyzed by *Xu and Cheng* [2016] were based on a higher-order turbulence closure [*Cheng and Xu*, 2006]. The latter approach produces more realistic subgrid-scale transports and fractional cloudiness in the embedded CRMs [*Cheng and Xu*, 2008].

The motive of this study is to understand the differences in HS between two MMFs that arise from the different treatments of turbulence and low clouds in order to aid to the understanding of the simulated HS spread among conventional GCMs [e.g., *DeAngelis et al.*, 2015, 2016; *Oueslati et al*., 2016; *Samset et al*., 2016]. As mentioned earlier, the intermodel spread in HS is related to both cloud and surface sensible heat flux feedbacks [e.g., *Previdi*, 2000] although difference in radiative transfer calculation is also a critically important factor [e.g., *Ogura et al.*, 2004; *DeAngelis et al.*, 2015]. In this study, cloud processes are explicitly represented and radiative transfer calculation is identical in the MMFs but the differences between them are solely due to the different treatments of turbulence. Conventional GCMs differ in parameterizations of cloud processes, turbulence and radiative transfer. The different treatments of turbulence in MMF also impact cloud processes because the higher-order turbulence closure acts as a unified parameterization of turbulence and low clouds [*Cheng and Xu*, 2006] and possibly the regional circulations that are tightly coupled to cloud processes.

The response of climate change caused by the increase of CO_2 concentration in the atmosphere involves direct and indirect effects; the direct effect is the rapid adjustment to the radiative heating due to the increased CO_2, while the indirect effect is the slow response to the CO_2 caused change of surface air temperature (SAT) [e.g., *Andrews et al.*, 2010; *Bony et al.*, 2013; *Kamae et al.*, 2015; *Fläschner et al*., 2016; *Oueslati et al*., 2016]. In this study, we will discuss the differences in the fast and slow precipitation responses to climate changes simulated by these two MMFs in atmosphere-only experiments with fixed SSTs. Two types of idealized experiments, one with prescribed SST perturbations and another with abrupt CO_2 increases, will be analyzed. The primary objective of this study is to understand the differences in the global, tropical, ocean and land mean hydrological sensitivity between two MMFs and the roles of turbulent transports in the hydrological cycle. It is beyond the scope of this study to examine mechanisms for local precipitation responses. The results will be helpful to re-interpret the potential causes of the model spreads among conventional GCMs that have been investigated from model ensembles with different experimental designs [e.g., *Stephens and Ellis,* 2008; *DeAngelis et al.*, 2015, 2016; *Mauritsen and Stevens,* 2015; *Fläschner et al*., 2016]. In other words, some of the plausible interpretations for the inter-model spreads may be confirmed by the findings presented in the present study.

2 Models and experiments

In the context of global climate modeling, the multiscale modeling framework (MMF) consists of a host GCM and an embedded CRM in each GCM grid column. The host GCM is the Community Atmosphere Model (CAM) Version 3.5 (CAM3.5) with the finite-volume dynamical core [*Collins et al*., 2006]. The newer versions of CAM have the same dynamical core as that in CAM3.5 and the MMF is not impacted by the improvements of the host GCM [*Wang et al.*, 2015]. The embedded CRM is a 2-D version of the System for Atmospheric Modeling (SAM), which is described in detail by *Khairoutdinov and Randall* [2003]. The standard SAM with a low-order turbulence closure is used in SPCAM (super-parameterized CAM) MMF. In SPCAM-IPHOC, SAM has been upgraded with an intermediately prognostic higher-order turbulence closure, IPHOC, to better represent boundary layer turbulence and low clouds [*Cheng and Xu*, 2006, 2008, 2011].

In MMF, the physical processes such as convection and stratiform cloudiness, usually parameterized in a conventional GCM, are resolved explicitly (but crudely) on the CRM fine grid cells. All CRMs have 32 grid columns with 4 km of horizontal grid spacing. Cloud microphysics and radiation are parameterized at the CRM scale. Tendencies of heat and moisture from the CRM scale communicate to the large scale via the GCM. The dynamical core provides the large-scale advective tendencies to the CRMs.

The sub-CRM-grid-scale variability is represented by IPHOC. IPHOC assumes a joint double-Gaussian distribution of liquid water potential temperature, total water, and vertical velocity [*Cheng and Xu*, 2006]. The properties of the double-Gaussian probability density function (PDF) are determined from the first-, second-, and third-order moments of the variables given above, and the PDF is used to diagnose cloud fraction and grid-mean liquid water mixing ratio, as well as the buoyancy terms and fourth-order terms in the equations describing the evolution of the second- and third-order moments.

The details of the experiment design were given in *Bretherton et al*. [2014] for SPCAM and *Xu and Cheng* [2013a, 2016] for SPCAM-IPHOC, respectively. Briefly, the MMF was forced by specifying climatological SST and sea ice distributions from Hadley Centre Sea Ice and Sea Surface Temperature dataset (HadISST) [*Rayner et al*., 2003] in SPCAM-IPHOC, but from the SST and sea ice dataset within CAM [*Hurrell et al.*, 2008] in SPCAM, with monthly-mean annual cycles. In SPCAM-IPHOC, the GCM has a horizontal grid size of 1.9°×2.5° (also for SPCAM) and there are 32 layers in the vertical with 12 of them below 700 hPa. The extra 6 layers below 700 hPa are used to better resolve the structures of stratocumulus clouds, compared to the SPCAM configuration used in *Wyant et al*. [2006, 2012] and *Bretherton et al*. [2014]. The embedded CRMs have the same vertical levels as the host GCM. The SPCAM-IPHOC simulations were integrated for 10 years and 3 months. The results from the last nine years are analyzed in this study. For the SPCAM simulations, the integration length is 35 years, with the analysis performed over years 2-10 to match with the analysis period of SPCAM-IPHOC simulations. These simulations are referred to as control.

Two sensitivity experiments were performed with SPCAM and SPCAM-IPHOC to study climate sensitivity, cloud response and precipitation change. One of the sensitivity experiments doubles the CO_2 concentration of present-day climate [*Hansen et al*., 1984], hereafter, 2xCO_2, for SPCAM-IPHOC but quadruples the CO_2 concentration for SPCAM (4xCO_2). The other experiment increases the SSTs uniformly by 2 K, hereafter, +2K, for SPCAM-IPHOC and by 4 K for SPCAM (+4K) [*Cess et al*., 1990]. The SST and sea ice are fixed but land surface temperature is allowed to change in both sets of experiments. The SPCAM results will be scaled to 2xCO_2 and +2K from 4xCO_2 and +4K experiments, respectively, by assuming a linear forcing-feedback relationship. Such scaling was widely applied in previous studies on climate sensitivity and cloud feedback [e.g., *Andrews et al.*, 2012].

As described earlier, the simulations from SPCAM and SPCAM-IPHOC also differ in the vertical resolution in the lower troposphere. The difference in precipitation rate is approximately 1% when the number of vertical layers below 700 hPa is changed from 6 to 12 for either SPCAM or SPCAM-IPHOC. The difference between the two MMFs is also less than 1% for the same number of vertical layers (Table 1). The two sensitivity tests, SPCAM with 12 layers, and SPCAM-IPHOC with 6 layers, were only run for two years and three months [*Xu and Cheng*, 2013b]. The comparison shown in Table 1 is based on the two-year averages of these two simulations and the control runs with SPCAM (6 layers) and SPCAM-IPHOC (12 layers). The difference between the two control runs is the smallest (~0.00 mm day^{-1}) among the pairs of simulations. Therefore, we conclude that the precipitation sensitivity is unlikely to be impacted by the different vertical resolutions employed by the two MMFs.

3 Results

3.1 The global energetic balance from the control runs

The surface energy budget components, i.e., SH, net surface LW flux and net surface SW flux, contribute to the energetic constraint. While the surface energy budget is not closed in these AGCM simulations, we now consider the individual components of the energetic constraint and its residual in the control simulations. Table 2 shows the individual energetic components of Eq. (1) averaged over the entire globe and its residual, which is defined as $H = LWC - LP - SWA - SH$, for the control runs. Table 2 includes clearsky LWC and SWA and the top-of-the-atmosphere (TOA) and surface cloud radiative effects (CREs), as well as total cloud amount, liquid water path (LWP) and ice water path (IWP). Observations of TOA and surface radiative fluxes and CREs from Clouds and the Earth's Radiant Energy System (CERES; *Loeb et al.*, 2009) are also listed, based upon the recently updated TOA and surface fluxes (Edition 4.0;

https://eosweb.larc.nasa.gov/project/ceres/ceres_table). The CREs are defined as the differences in radiative fluxes between the clear and all skies.

SWA has the smallest difference among the individual components between the two MMFs (0.1 W m^{-2}), followed by latent heating (-0.3 W m^{-2}). Surface sensible heat flux is higher in SPCAM-IPHOC by 2.9 W m^{-2} while LW cooling has the second highest difference (1.2 W m^{-2}) between the MMFs. The increase in the surface sensible heat flux dominates the residual (H) change from -0.9 W m^{-2} in SPCAM to -2.4 W m^{-2} in SPCAM-IPHOC while the latent heating is kept roughly the same. Both residuals are smaller than the differences between the MMFs and CERES observations in all-sky LW cooling, LW and SW CREs at TOA and surface but they are comparable to those in clearsky and all-sky SWAs (Table 2). The CREs of SPCAM-IPHOC are generally closer to the CERES observations than those of SPCAM, in particular, the surface CREs. This means that the inclusion of IPHOC also greatly impacts and improves the simulation of clouds and their radiative effects due to the fact that the simulated clouds are optically thinner and their areal coverage is larger than in SPCAM but it has no significant impact on global-mean precipitation of the control simulations [Table 2; *Xu and Cheng*, 2013a].

3.2 The local responses of precipitation and energetic components in the tropics

Before discussing the statistical results for the global, tropical, tropical land and tropical oceanic means, the geographic distributions of individual energetic components are explained. Figure 1 shows the precipitation (multiplied by the latent heat of vaporization) distributions between 30°S and 30°N from the control, +2K and 2xCO_2 simulations of SPCAM-IPHOC. The similar results for the control, +4K and 4xCO_2 simulations of SPCAM are shown in Figure 2. The precipitation patterns of the control experiments in the tropics are similar between the two MMFs and comparable to observations [*Huffman et al.*, 2009] but by no means agree perfectly.

The MMFs do not produce double intertropical convergence zones (ITCZs) that plague most of conventional GCMs, especially the coupled ocean-atmosphere models [e.g., *Lin*, 2007], and various versions of CAM [e.g., *Xie et al.*, 2012]. In the MMFs, the ITCZ precipitation bands are also narrower in the central and eastern Pacific and Atlantic than in the western Pacific. Precipitation intensity increases in +2K and +4K simulations (hereafter, "+SST" simulations) but decreases in 2xCO_2 and 4xCO_2 simulations (hereafter, "xCO_2" simulations), but not uniformly in space. The increase/decrease in intensity is accompanied by an expansion/shrinking of precipitation areas. A noticeable difference between the two MMFs is the presence of a weak precipitation zone over the eastern Pacific south of the equator in all three experiments performed with SPCAM-IPHOC. This is due to the different SST datasets used in the two MMFs. As discussed in *Xu et al.* [2013b], this weak ITCZ is only simulated over the warm SST areas during the boreal spring.

Figures 3-6 show the geographic distributions of the differences between the sensitivity and control experiments for latent heating, LWC, SWA, *SH* and convergence of dry static energy flux (H). H is vertically integrated net convergence of dry static energy flux but is diagnosed as the residual from the other four terms in the energetic constraint equation. The differences are scaled to +2K and 2xCO_2 for SPCAM. Spatial correlations between latent heating and LWC (or SWA, SH, H) over the entire tropics are listed over panels (b-e) and Table 3. As stated earlier, it is beyond the scope of this study to examine the details of physical mechanisms for the local response [e.g., *Charwick et al.,* 2013; *DeAngelis et al.,* 2016].

For +SST experiments (Figures 3 and 4), precipitation increases over the oceanic areas with strong precipitation but decreases over the oceanic areas with weak precipitation of the control experiments (Figures 1a and 2a). This is known as the "rich get richer" mechanism [e.g., *Chou and Neelin*, 2004]. The spatial correlation over the tropics between the precipitation change and mean precipitation of the control experiment is 0.49 and 0.56 for SPCAM and SPCAM-IPHOC (Table 3), respectively, compared to 0.2 of the CMIP5 multi-model ensemble [*Charwick et al.*, 2013]. Over most of south America and Africa as well as parts of northern Asia, precipitation decreases, which is correlated with warming due to convergence of dry static energy flux and increase in SH. This is also the case over eastern Australia and the adjacent ocean in SPCAM-IPHOC. However, precipitation over the same region increases in SPCAM, which is related to cooling due to decrease in SH over lands and to divergence of dry static energy flux over the oceanic area. Precipitation over the eastern Pacific south of the equator increases slightly more in SPCAM-IPHOC than in SPCAM due to, as mentioned earlier, the higher SSTs there resulting from the use of two different SST datasets in the two MMFs.

The regional patterns of precipitation changes are positively (0.21-0.27) correlated with those of SWA changes (but higher over lands, 0.38-0.40; Table 3) due to cloud radiative cooling. The weak correlation is due to the fact that cooling change can be large in low cloud regions but with negligible precipitation change. Although LWC is, as discussed later, a major contributor to the precipitation change over the entire tropics/globe, the regional patterns of LWC changes are negatively correlated with those of precipitation changes (-0.47 for SPCAM, -0.53 for SPCAM-IPHOC) due to cloud radiative heating in the precipitating regions. The correlation is weaker over lands (-0.08 for SPCAM, -0.22 for SPCAM-IPHOC; Table 3). Changes in SH are small over the ocean (-5 to 0 W m^{-2}) but larger over lands. They are weakly and negatively (-0.16 - -0.26) correlated with precipitation changes due to the stronger negative correlations over lands (-0.52 - -0.58; Table 3). Thus, the closer matching in the spatial patterns (correlation of nearly 1.00) and the larger magnitudes of change suggest that the regional patterns of precipitation changes are largely determined by those of changes in divergence of dry static energy flux ($-H$). Note that SPCAM-IPHOC has finer spatial patterns in both precipitation and H changes than SPCAM over the entire tropics. This is likely related to larger circulation changes resulting from the higher amplitude of SST perturbations in SPCAM (+4 K vs. 2 K).

For xCO_2 experiments, the most pronounced feature of the precipitation responses is the increased precipitation over tropical land areas as noted by *Wyant et al.* [2012] and seen in Figures 5a and 6a, though SPCAM-IPHOC does have weak decreases in precipitation over parts of equatorial Africa and South America. Precipitation decreases over most of the oceanic regions except for the equatorial Pacific due to slight southward movement of the ITCZ. Over Asia, Australia and non-equatorial Africa and equatorial western Pacific, the increases in precipitation are larger in SPCAM-IPHOC than in SPCAM. The larger increases over these regions are responsible for a smaller tropical-mean precipitation reduction in SPCAM-IPHOC than in SPCAM. The local fast precipitation response is mostly opposite to that of slow response (Table 3) because of the direct radiative heating due to CO_2 increase and the resulting changes in atmospheric circulations over the ocean and lands.

The longwave warming (negative values in Figures 5d and 6d) from increased CO_2 is a major contributor to the precipitation reduction over the entire tropics/globe. Similar to +SST experiments, the regional patterns of LWC/SWA changes are negatively/positively correlated (-0.64/0.52 for SPCAM and -0.46/0.54 for SPCAM-IPHOC) with those of precipitation changes due to cloud radiative heating/cooling. As in +SST experiments (Figures 3c and 4c), the dominant contributor to the local precipitation response is the change in convergence of dry static energy flux. However, the two MMFs do not agree on the signs of SH changes over some parts of the oceanic areas and parts of Asia, Australia and equatorial Africa, as indicated by their correlations of -0.11 for SPCAM-IPHOC and 0.20 for SPCAM with precipitation changes. This result is related to much stronger negative correlation over lands (-0.61 vs. -0.21) and stronger positive correlation over the ocean (0.27 vs. 0.14) in SPCAM-IPHOC than SPCAM (Table 3).

3.3 The global hydrological response

The global mean precipitation rates averaged over nine years from the control simulations are very close (2.87 mm day^{-1} for SPCAM and 2.86 mm day^{-1} for SPCAM-IPHOC), but higher than observations (2.62 mm day^{-1}) [*Huffman et al*., 2009]. The hydrological cycle response from +SST experiments is a precipitation increase of 3.0% K^{-1} for SPCAM and 3.6% K^{-1} for SPCAM-IPHOC, respectively. Both are significantly higher than those simulated from +SST experiments of conventional AGCMs, 2.52±0.22% K^{-1} [e.g., *Allan et al*., 2014; *Andrews et al*., 2010; *Samset et al*., 2016] albeit the configurations of experiments are different. For example, AGCM experiments used a simple slab ocean model and the slow response is diagnosed from the difference between the total and fast responses, whereas the fast response experiments are configured identically as in the present study [*Andrews et al.*, 2010; *Kvalevåg et al.*, 2013; *Samset et al.*, 2016]. The difference of 0.6% K^{-1} between the two MMFs is very close to the spread of the slow responses among conventional AGCMs. All of these responses lie within the observationally based estimate of 2.83±0.92% K^{-1} for the period 1988-2008 [*Allan et al*., 2014] with SPCAM-IPHOC being at the upper end of the range. It is, however, cautioned that the observational estimate was based upon a regression of global mean precipitation to interannual anomalies of SAT (Table 4), which are not simulated with Cess-type experiments performed with MMF but are simulated with conventional AGCM’s AMIP experiments with interannual variability of SSTs and sea ice [*Allan et al.*, 2014].

Fläschner et al. [2016] defined the hydrological sensitivity analogous to the equilibrium climate sensitivity framework. This sensitivity for +SST experiments is calculated as the ratio of the changes in latent heating (precipitation) to those in SAT. The hydrological sensitivity is 2.50 W m^{-2} K^{-1} for SPCAM and 2.96 W m^{-2} K^{-1} for SPCAM-IPHOC. Both MMFs lie within the range of 2.79±0.26 W m^{-2} K^{-1} from +4K SST experiments of conventional AGCMs according to this definition of hydrological sensitivity (Table 4). But the difference of 0.46 W m^{-2} K^{-1} between the MMFs suggests that changing only the turbulence parameterization in an MMF can lead to substantial changes in hydrological sensitivity.

In the following, we will instead use the fractional precipitation changes to consistently scale the precipitation responses between +SST and xCO_2 sets of experiments. The fast responses from xCO_2 experiments are stronger for SPCAM with a fractional precipitation change of -2.66% vs. -2.05% for SPCAM-IPHOC, compared to -2.5±0.4% from $2xCO_2$ experiments of conventional AGCMs [*Samset et al*., 2016]. For +SST experiments, the fractional precipitation changes are 6.83% for SPCAM and 7.90% for SPCAM-IPHOC, respectively, compared to 6.0±1.6% for conventional AGCMs [*Samset et al*., 2016]. Therefore, the precipitation sensitivity in SPCAM-IPHOC is stronger (+1%) for the slow response but weaker for the fast response (-0.6%) than both SPCAM and the ensemble mean of conventional AGCMs for similar (but identical for xCO_2) experiment configurations. For comparison, the host GCM of the MMFs, CAM4, produces a slow response of 7.6±0.3% and a fast response of -2.3±0.2% [*Kvalevåg et al.*, 2013].

Why are the precipitation changes different between the MMFs even though they differ only in the representation of turbulence in the embedded CRMs? Do the differences result from changes in cloud-induced radiative heating or surface turbulent fluxes? To address these questions, the changes in the energetic constraint components shown in (1) are normalized by the mean latent heating of the respective MMF control simulation over a region (e.g., the globe/tropics), which are shown in Figures 7 and 8, as well as Tables 5 and 6 with additional parameters such as clearsky SW heating and LW cooling, CREs and convergence of dry static energy flux (ΔH). The changes (Δ) in the energetic components between the sensitivity and control experiments are linked through the following equation:

$$\Delta LWC/L\bar{P} = (L\Delta P + \Delta SWA + \Delta SH + \Delta H)/L\bar{P}, \tag{2}$$

where $\bar{P}$ is the averaged surface precipitation rate of the control experiments of either SPCAM or SPCAM-IPHOC. For the global-mean energetic changes to be discussed below, ΔH is the change in the residual that is due to the unclosed surface energy budget as discussed earlier in section 3.1.

The changes in the energetic components are similar in several aspects between the two models. First, LWC is the largest term in contributing to the increases of precipitation for +SST experiments. This is also true for xCO_2 experiments except for LW warming due to increased CO_2 that contributes to the decreases of precipitation. Second, the magnitudes of ΔLWC are, at least, 1% higher than that of precipitation sensitivity for +SST experiments (Figure 7) but only slightly smaller for xCO_2 experiments (Figure 8). Third, increased heating (ΔSWA) cancels out approximately one-fourth of ΔLWC contribution of +SST experiments but contributes little to the decrease of precipitation of xCO_2 experiments. Such relationships between the precipitation sensitivity and changes in LWC/SWA are opposite to those in the local precipitation responses discussed earlier in section 3.2. Finally, both ΔSH and ΔH are small (but not negligible) contributors to the energetic constraint, compared to ΔLWC (Tables 5 and 6), which will be further discussed shortly.

The difference in the global-mean precipitation changes between SPCAM-IPHOC and SPCAM is 1.07% for +SST experiments. The higher precipitation sensitivity in SPCAM-IPHOC is contributed by more LWC (0.59%), lower SH heating (0.32%) and more cooling due to ΔH (0.28%) but the slightly higher SWA heating reduces the precipitation sensitivity by 0.12%. Due to the negligible differences in clearsky SWA (0.03%) and LWC (0.02%) changes, the difference in CRE changes is, as discussed later, a major contributor to the higher precipitation sensitivity in SPCAM-IPHOC. In Eq. (2), magnitudes of ΔSH are smaller than those of either ΔLWC or ΔSWA for both MMFs, in agreement with previous studies [e.g., *Held and Soden*, 2006; *Lu and Cai*, 2009], but ΔSH is responsible for a significant portion of the differences in the slow (0.32% out of 1.07%) and fast (0.52% out of 0.62%) precipitation responses between the MMFs (Tables 6 and 7). For example, the sign of ΔSH for the fast responses is opposite between the two models. The increase in SH heating (0.39%) contributes to a larger reduction in surface precipitation in SPCAM, i.e., a stronger precipitation response to increased CO_2, compared to the decrease in SH heating (-0.13%) for SPCAM-IPHOC. As discussed later, ΔSH over the tropical lands in SPCAM is ~12 times larger than that in SPCAM-IPHOC because overheated lands from CO_2 warming produce large increase in SH (see Figures 5b and 6b) coupled with large decrease in surface latent heat (LH) flux, likely due to the lack of low-level clouds and precipitating clouds in SPCAM.

Does the change in the residual (ΔH) alter the precipitation responses? The absolute magnitudes of ΔH in either set of experiments are smaller in SPCAM than in SPCAM-IPHOC, which is consistent with the smaller residual in the control experiment of SPCAM (Table 2). The differences in ΔH between the two MMFs contribute a small proportion in the precipitation sensitivity (0.28% out of 1.07% for the slow response; 0.18% out of 0.62% for the fast response), in comparison with those of ΔLWC in +SST experiments (0.59%) and ΔSH in xCO_2 experiments (0.52%). Therefore, the unclosed surface energy balances in these MMFs do not change the sign of the difference in the global-mean HS between the two MMFs albeit they are not negligibly small. However, the impact of this imbalance on the energetic constraint was not discussed in the earlier AGCM studies [e.g., *Fläschner et al*., 2016; *Samset et al*., 2016].

As discussed above, a major factor for determining the HS is the changes in net radiative cooling/warming (*Stephens and Ellis*, 2008; *Stephens and Hu*, 2010). How different are the two MMFs in this regard? The ratios of ΔR_{ATM} (ΔLWC - ΔSWA) to change in SAT (ΔT) of +SST experiments, i.e., 2.24 W m^{-2} K^{-1} for SPCAM and 2.47 W m^{-2} K^{-1} for SPCAM-IPHOC (Table 4), are higher than conventional GCMs, 1.92 ± 0.16 W m^{-2} K^{-1} [*Allan et al.*, 2014]. *Mauritsen and Stevens* [2015] tried to explain the muted precipitation response in conventional AGCMs with the lack of the iris effect, an expansion of clearsky area with warming. Although relatively low ECS and relatively high HS of the AGCM simulations with SPCAM and SPCAM-IPHOC seem supportive of *Mauritsen and Stevens* [2015], these uncoupled simulations are not directly comparable to those in that paper. A coupled simulation with SPCAM [*Bretherton et al.*, 2014] has a slightly lower HS (2.7% K^{-1} vs. 3.0% K^{-1}) and a higher ECS (2.8 K vs. 2.1 K) than the uncoupled counterpart. The relatively large HS in SPCAM and SPCAM-IPHOC may be related to a stronger precipitation response to changes in net atmospheric radiative cooling. In fact, the ratio of $L\Delta P$ to ΔR_{ATM} of SPCAM (1.12) and SPCAM-IPHOC (1.20) is closer to observationally based estimate (1.09 ± 0.17) for the period 1998-2008 than that in conventional GCMs (0.83 ± 0.03; *Allan et al*. [2014]), though this comparison is only qualitative because of the different configurations of AGCM and MMF simulations and the uncertainties in precipitation measurements and re-analysis data.

The higher $L\Delta P/\Delta R_{ATM}$ in SPCAM-IPHOC is due to the higher decreasing rate of surface SH with surface warming (Figure 7) than in SPCAM, which will be discussed shortly. The higher values in both ratios ($\Delta R_{ATM}/\Delta T$ and $L\Delta P/\Delta R_{ATM}$) help increase the HS in +SST experiment of SPCAM-IPHOC. For xCO_2 experiments, $L\Delta P/\Delta R_{ATM}$ is much higher in SPCAM (1.21) than in SPCAM-IPHOC (0.89), which explains the higher sensitivity in SPCAM. This large difference is, as discussed earlier, due to the effect of SH changes with opposite signs on the precipitation decrease, agreeing with *DeAngelis et al.* [2016] regarding significant spreads in ΔSH for conventional GCMs. These results indicate that SH changes, importance of which has recently been highlighted [*Stephens and Hu*, 2010; *O'Gorman et al.*, 2012; *DeAngelis et al.*, 2016; *Fläschner et al.*, 2016; *Kramer and Soden*, 2016], play an important role in determining the precipitation sensitivity for both the slow and fast responses.

What role do clouds play in producing the higher HS in SPCAM-IPHOC than in SPCAM? Changes in the clearsky LWC (10.63%, 10.65%) and SWA (2.75%, 2.72%) are nearly identical between the two MMFs for +SST experiments. The relatively larger change in net cloud radiative heating (1.78% for SPCAM; 1.35% for SPCAM-IPHOC; Table 5) is thus responsible for smaller $\Delta R_{ATM}/\Delta T$ in SPCAM because of the similar clear-sky $\Delta R_{ATM}/\Delta T$. The lack of low clouds in the control simulation enhances the sensitivity of cloud radiative heating in SPCAM and conventional AGCMs because cloud changes are dominated by those of high clouds, compared to SPCAM-IPHOC, as seen from the larger LW cloud heating change relative to SW cloud cooling change in SPCAM (Table 5). Further, the differences in cloud radiative heating sensitivity between the two MMFs are similar for +SST and xCO_2 experiments (0.43% vs. 0.48%). In xCO_2 experiments (Table 6), the positive cloud heating sensitivity in SPCAM

(0.19%) reduces precipitation more than that attributed to clearsky CO_2 heating increase. The opposite is true for SPCAM-IPHOC (-0.29%).

A greater reduction in surface SH fluxes that are associated with a more stable boundary layer [*Lu and Cai*, 2009] in +SST experiment of SPCAM-IPHOC is related to a greater HS (Figure 9), which leads to a higher ratio of $L\Delta P$ to ΔR_{ATM} by 0.09 over SPCAM. The LH flux directly impacts the HS through the water budget, which is larger in SPCAM-IPHOC than in SPCAM. The greater reduction in SH causes a larger fractional decrease in the Bowen ratio (SH/LH) with surface warming, which is about 6.5% K^{-1} for SPCAM-IPHOC but is less than 5.0% K^{-1} for SPCAM. (The fractional changes shown in Figure 9 are divided by ~2.2 K.) Thus, the inclusion of IPHOC in MMF exerts a greater influence on the response of boundary-layer turbulent transports to surface warming, in particular, with stronger stabilization of boundary layer. The higher vertical resolution in the boundary layer of SPCAM-IPHOC may also play a role. Unlike conventional GCMs, the wind gustiness that impacts surface fluxes is directly simulated in MMF. One would expect IPHOC to have significant impacts on boundary-layer turbulent transports though it might not be clear which sign it would have on the HS relative to low-order turbulence closures used in SPCAM and conventional GCMs.

As discussed in *Stephens and Hu* [2010], the sensitivity of net cloud radiative heating is opposite in sign with that of surface SH flux. If they canceled out with each other, the precipitation sensitivity would be determined by that of clearsky radiative cooling ($\Delta(R_{ATM})_{clr}$). Because the sensitivity of SH flux is lower in SPCAM, it cannot compensate the higher sensitivity of net cloud radiative heating. Therefore, precipitation sensitivity in SPCAM is far less than that due to clearsky radiative cooling, compared to SPCAM-IPHOC (Table 4). The ratio of $L\Delta P$ to clearsky ΔR_{ATM} is 0.87 for SPCAM but 0.99 for SPCAM-IPHOC. Therefore, the substantial improvements in the simulation of low-level clouds and turbulence in SPCAM-IPHOC [*Cheng and Xu*, 2011, 2013a, b; *Xu and Cheng*, 2013a, b; *Painemal et al.*, 2015] play a major role in enhancing the precipitation sensitivity.

3.4 The tropical and regional hydrological responses

In this study, the Tropics is defined as the area between 30°S and 30°N, representing half the area of the Earth's surface. The hydrological changes in the tropics generally mirror those of the entire globe for both MMFs, only weaker for +SST runs but slightly stronger for xCO_2 runs. The differences from those of the globe are similar in SPCAM-IPHOC (-0.90%, slow response; -0.18%, fast response) and SPCAM (-0.70%, slow response; -0.13%, fast response) (Tables 5 and 6). The weaker sensitivity in the tropics is attributed largely to a weaker sensitivity of LW radiative cooling to SST increase (Figure 7). The stronger sensitivity of clear-sky LW radiative heating to CO_2 increase is responsible for the higher precipitation sensitivity in xCO_2 runs (and so is that of SH flux for SPCAM) because other terms in the energetic budget act to reduce the sensitivity relative to that of the global mean (Table 8).

The land and oceanic parts of the Tropics (26% land and 74% ocean) are now considered separately. The convergence of dry static energy flux is a significant contributor in the regional energy budget [e.g., *Muller and O'Gorman*, 2011], and it is one of the largest contributors to the tropical hydrological cycles over lands (Tables 5 and 6). The geographic patterns of ΔH are shown in Figures 3-6 and matched to those of ΔP perfectly. The signs of regional-mean ΔH (Tables 5 and 6) are consistent between the two MMFs; i.e., convergence over the tropical lands in the slow responses but divergence in the fast responses. The signs are reversed and their magnitudes are smaller over the tropical ocean. The differences in ΔH between SPCAM-IPHOC and SPCAM are 1.42% (fast response) to -1.07% (slow response) over lands but -0.05 (slow response) to 0.04% (fast response) over the ocean, suggesting that changes in land-ocean transports can impact the precipitation response over lands.

The reduction (increase) of tropical land precipitation agrees qualitatively with conventional GCMs for the slow (fast) responses [e.g., *Samset et al*., 2016; *DeAngelis et al.*, 2016]. The tropical land precipitation experiences 2.79% reduction for SPCAM, but only 0.55% reduction for SPCAM-IPHOC in +SST simulations, compared to their respective control simulations. In xCO_2 simulations, the tropical land precipitation increases by 2.65% for SPCAM but 5.11% for SPCAM-IPHOC (Figures 7 and 8). These differences between the two MMFs are on par with significant intermodel variability over lands simulated by conventional GCMs [*Samset et al*., 2016; *DeAngelis et al.*, 2016].

Why does IPHOC greatly increase the tropical land precipitation? What causes such large differences between the two MMFs? SPCAM has much larger increases in ΔSH (3.57% and 4.83% for +SST and xCO_2 simulations, respectively) than in SPCAM-IPHOC (2.80% and 0.39%). In $4xCO_2$ simulation ΔSH is 12 times as large as that in $2xCO_2$ simulation, which is compensated by a large reduction in LH in SPCAM. This difference implies that the land surface is heated up more easily, the boundary layer is deeper and deep convection produces less surface precipitation due to the drier/warmer boundary layer in SPCAM. There is evidence to support this explanation. Low and total cloud fractions over the tropical lands increase in $2xCO_2$ experiment of SPCAM-IPHOC (0.17%, 1.20%), compared to low cloud reduction (-0.45%) and smaller increase in total cloud fraction (0.40%) in $4xCO_2$ experiment of SPCAM. For +SST simulations, tropical lands in SPCAM experience larger reductions in low (-1.54% vs. -0.91%) and total (-2.35% vs. -1.39%) cloud fractions than those in SPCAM-IPHOC.

As shown in Tables 5 and 6, the differences in ΔSH (0.77%) and ΔH (1.07%; divergence) contribute to the difference in precipitation reduction (2.24%) over tropical lands in +SST simulations between the MMFs, with a smaller contribution from ΔR_{ATM} (0.40%; cooling). In xCO_2 simulations, the difference in ΔSH contributes to the difference in precipitation increase (4.44% of 2.46%), which is compensated by the differences in ΔH (-1.42%; convergence) and ΔR_{ATM} (-0.56%; warming). The difference in ΔR_{ATM} is largely contributed by that in ΔCRE. For tropical oceanic regions, the slightly higher sensitivity in SPCAM-IPHOC relative to SPCAM (+0.72%) can be attributed to the stronger net radiative cooling (+0.63%) for the slow response. A cancellation of a higher reduction in surface SH flux (0.24%) with ΔR_{ATM} (warming; -0.29%) results in a negligible difference in the precipitation sensitivity for the fast response.

4 Summary and discussion

The MMFs simulate less muted global hydrological response with surface warming than conventional GCMs [e.g., *Allan et al.*, 2014; *Andrews et al.*, 2010; *Samset et al.*, 2016]. The lower hydrological sensitivity of conventional GCMs could be associated with inadequate representation of both turbulence and cloud processes [*Mauritsen and Stevens*, 2015]. SPCAM-IPHOC with a higher-order turbulence closure simulates higher global hydrological sensitivity for the slow response but lower sensitivity for the fast response, compared to SPCAM with a low-order turbulence closure. The differences in the fractional precipitation change of 1% (or 0.6% K^{-1}) for the slow response and 0.6% for the fast response between the two MMFs are close to the spreads of conventional GCMs with similar/identical experimental designs as in this study [*Samset et al*., 2016; *Fläschner et al*., 2016], though the intermodel spreads for fully coupled GCMs can be higher [e.g., *DeAngelis et al.*, 2015]. These differences have been examined according to the energetic constraint in this study to help understand the potential causes of model spreads among conventional GCMs. The discussion presented below is subject to this caveat. The individual components are expected to compensate each other so that the causes for the difference in the hydrological sensitivity cannot be fully isolated.

It is found that changes in longwave radiative cooling (ΔLWC) contribute half of the difference in precipitation sensitivity between the two MMFs with surface warming (i.e., the slow response), which is related to higher sensitivity of cloud radiative heating in SPCAM, because the sensitivity of clearsky LWC is nearly identical. This result is related to the lack of low clouds in SPCAM (and conventional GCMs). The cloud radiative heating sensitivity is enhanced because cloud changes are attributed to those of high clouds, compared to SPCAM-IPHOC. On the other hand, the more stable boundary layer simulated by SPCAM-IPHOC is responsible for a greater reduction in surface sensible heat flux with surface warming. This contributes one third of the difference in precipitation sensitivity between the two MMFs for the slow response although magnitudes of ΔSH are smaller than those of other energetic components. The rest is contributed by higher sensitivity of cooling due to the surface energy budget imbalance but offset by higher sensitivity of SW radiative heating in SPCAM-IPHOC. For the fast response, the difference in ΔSH is responsible for most of the difference in precipitation sensitivity between the two MMFs. The large increase in SH (but compensated by LH decrease) is responsible for stronger precipitation reduction in SPCAM. Partitioning between SH and LH over lands in SPCAM-IPHOC is drastically different with small increases in both SH and LH. It is not clear whether these differences are related either to the vegetation responses [*DeAngelis et al.,* 2016] or the different formulations of boundary-layer turbulent processes.

It is also found that the fractional precipitation (latent heating) change is nearly equal to the fractional clearsky net radiative cooling in SPCAM-IPHOC (0.99) but less in SPCAM (0.87).

A theoretical ratio is 1.00 (e.g., *Stephens and Hu*, 2010). The ratio of the changes in latent heating to those in all sky net radiative cooling ($L\Delta P/\Delta R_{ATM}$) is higher for SPCAM-IPHOC (1.20) than for SPCAM (1.12), and so is ΔR_{ATM} with surface warming ($\Delta R_{ATM}/\Delta T$) (2.24 W m^{-2} K^{-1} for SPCAM and 2.47 W m^{-2} K^{-1} for SPCAM-IPHOC). The higher values of both ratios in SPCAM-IPHOC help to explain the muted precipitation response in conventional GCMs, which have much lower values (0.83$\pm$0.03 and 1.92$\pm$0.16 W m^{-2} K^{-1}) than either MMF. For xCO_2 experiments, the higher $L\Delta P/\Delta R_{ATM}$ also explains the larger precipitation decrease in SPCAM than in SPCAM-IPHOC, due to the effect of SH changes with opposite signs in the two models. These results confirm that the SH changes due to stabilization of the boundary layer and less surface warming over lands due to the presence of low clouds and more precipitating clouds play an important role in determining the hydrological sensitivity, especially for the fast response [*Stephens and Hu*, 2010; *O'Gorman et al.*., 2012; *DeAngelis et al.*, 2016].

Furthermore, the difference in the SWA sensitivity is small between the two MMFs and that of its clearsky counterpart is even smaller due to the use of the same CAM4 radiation transfer code [*Mlawer et al.*, 1997] in the two MMFs. Therefore, the explanation based upon the clearsky SWA sensitivity with precipitable water [*DeAngelis et al.*, 2015] is not relevant to the differences in the hydrological sensitivity between the two MMFs discussed in this study. Even though the SWA sensitivity has a relatively small magnitude, as in the SH sensitivity, one cannot rule out its importance in explaining the model spreads in the hydrological sensitivity of conventional GCMs with different radiation transfer codes.

The two MMFs differ greatly in the hydrological sensitivity over the tropical lands, with SPCAM-IPHOC simulating much smaller reduction in precipitation for the slow responses and larger increase for the fast responses. The simulated sensitivity in surface SH fluxes with surface warming and CO_2 increase in SPCAM-IPHOC is weaker than in SPCAM (also partially related to partitioning of LH and SH because the sum of LH and SH is similar) but the difference in divergence of dry static energy flux also contributes to that in precipitation sensitivity between the two MMFs. The regional patterns of the divergence determine the regional precipitation changes but radiative forcing can damp or enhance the precipitation change. The change in the large-scale circulations is critically important for understanding the local and regional responses [*Bony et al.*, 2013; *Charwick et al.*, 2013; *Kamae et al.*, 2015; *Muller and O'Gorman*, 2011; *Oueslati et al.*, 2016], which require a more detailed analysis from the MMF simulations.

Acknowledgments: The lead author is supported by NASA Interdisciplinary Study program (Grant NNH12ZDA001N-IDS). The computational resources were provided by Argonne National Laboratory, DOE's Office of Science and the local computation clusters: K-cluster and Icluster. ZL acknowledges the support of NASA Postdoctoral Program. PNB and CS acknowledge support from the NSF Science and Technology Center for Multi-Scale Modeling of Atmospheric Processes (CMMAP), led by David Randall and managed by Colorado State University under cooperative agreement No. ATM-0425247. The SPCAM and SPCAM-IPHOC data are available on a public server (http://hdl.handle.net/1773/40329).

References

Allan, R. P., C. Liu, M. Zahn, D. A. Lavers, E. Koukouvagias, and A. Bodas-Salcedo (2014), Physically consistent responses of the global atmospheric hydrological cycle in models and observations, *Surv. Geophys.*, *35*, 533–552. doi:10.1007/s10712-012-9213-z.

Andrews, T., P. M. Forster, O. Boucher, N. Bellouin, and A. Jones (2010), Precipitation, radiative forcing and global temperature change, *Geophys. Res. Lett.*, *37*, L14701, doi:10.1029/2010GL043991.

Andrews, T., J. M. Gregory, M. J. Webb, and K. E. Taylor (2012), Forcings, feedbacks and climate sensitivity in CMIP5 coupled atmosphere-ocean climate models, *Geophys. Res. Lett.*, *39*, doi:10.1029/2012GL051607.

Arnold, N. P., M. Branson, M. A. Burt, D. S. Abbot, Z. Kuang, D. A. Randall, and E. Tziperman (2014), The effects of explicit atmospheric convection at high CO2, *Proc. Natl. Acad. Sci. U. S. A.*, *111*, 10,943–10,948, doi:10.1073/pnas.1407175111.

Bony, S., et al. (2013), Robust direct effect of carbon dioxide on tropical circulation and regional precipitation, *Nature Geoscience*, *6*, 447–451, doi:10.1038/ngeo1799.

Bretherton, C. S., P. N. Blossey, and C. Stan (2014), Cloud feedbacks on greenhouse warming in the superparameterized climate model SPCCSM4, *J. Adv. Model. Earth Syst.*, *6*, doi:10.1002/2014MS000355.

Cess, R. D., et al. (1990), Intercomparison and interpretation of climate feedback processes in 19 atmospheric general circulation model, *J. Geophys. Res.*, *95*, 16,601-16,615.

Chadwick, R., O. Boutle, and G. Martin (2013), Spatial patterns of precipitation change in CMIP5: Why the rich do not get richer in the tropics, *J. Clim.*, *26*, 3803-3822, doi:10.1175/jcli-d-12-00543.1.

Cheng A., and K.-M. Xu (2006), Simulation of shallow cumuli and their transition to deep convective clouds by cloud-resolving models with different third-order turbulence closures, *Q. J. Roy. Meteor. Soc.* *132*, 359-382.

Cheng A., and K.-M. Xu (2008), Simulation of boundary-layer cumulus and stratocumulus clouds using a cloud-resolving model with low and third-order turbulence closures, *J. Meteor. Soc. Japan*, *86A*, 67-86.

Cheng, A., and K.-M. Xu (2011), Improved low-cloud simulation from a multiscale modeling framework with a third-order turbulence closure in its cloud-resolving model component, *J. Geophys. Res.*, *116*, D14101, doi:10.1029/2010JD015362.

Cheng, A., and K.-M. Xu (2013a), Improving low-cloud simulation from an upgraded multiscale modeling framework model. Part III: Tropical and subtropical cloud transitions over the northern Pacific, *J. Climate*, *26*, 5761-5781.

Cheng, A., and K.-M. Xu (2013b), Diurnal variability of low clouds in the southeast Pacific simulated by an upgraded multiscale modeling framework model, *J. Geophys. Res.*, *118*, 9191-9208, doi:10.1002/jgrd.50683).

Chou, C., and J. D. Neelin (2004), Mechanisms of global warming impacts on regional tropical precipitation. *J. Climate*, **17,** 2688–2701.

Collins, W. D., et al. (2006), The formulation and atmospheric simulation of the Community Atmosphere Model Version 3 (CAM3), *J. Climate*, *19*, 2144–2161.

DeAngelis, A. M., X. Qu, M. D. Zelinka, and A. Hall (2015), An observational radiative constraint on hydrologic cycle intensification, *Nature*, *528*, doi:10.1038/nature15770.

DeAngelis, A. M., X. Qu, and A. Hall (2016), Importance of vegetation processes for model spread in the fast precipitation response to CO_2 forcing, *Geophys. Res. Lett.*, *43*, 12,550–12,559, doi:10.1002/2016GL071392.

Fläschner, D., T. Mauritsen, and B. Stevens (2016), Understanding the intermodel spread in global-mean hydrological sensitivity, *J. Clim.*, *29*, 801–817, doi:10.1175/jcli-d-15-0351.1.

Grabowski, W. W. (2001), Coupling cloud processes with the large-scale dynamics using the cloud-resolving convection parameterization (CRCP), *J. Atmos. Sci.*, *58*, 978–997.

Hansen, J., A. Lacis, D. Rind, G. Russell, P. Stone, I. Fung, R. Ruedy, and J. Lerner (1984), Climate sensitivity: Analysis of feedback mechanisms, in *Climate Processes and Climate Sensitivity*, *Geophys. Monogr. 29*, edited by J. E. Hansen and T. Takahashi, pp. 130–163, AGU, Washington, D. C.

Held, I. M., and B. J. Soden (2006), Robust responses of the hydrological cycle to global warming, *J. Climate*, *19*, 5686–5698, doi: 10.1175/JCLI3990.1.

Huffman G. J., R. F. Adler, D. T. Bolvin, and G. Gu (2009), Improving the global precipitation record: GPCP version 2.1, *Geophys. Res. Lett.*, *36*, *L17808*. doi: 10.1029/2009GL040000.

Hurrell, J. W., J. J. Hack, D. Shea, J. M. Caron, and J. Rosinski (2008), A new sea surface temperature and sea ice boundary dataset for the Community Atmosphere Model, *J. Climate*, *21*, 5145-5153, doi:10.1175/2008JCLI2292.1.

Kamae, Y., M. Watanabe, T. Ogura, M. Yoshimori, and H. Shiogama (2015), Rapid adjustments of cloud and hydrological cycle to increasing CO2: A review, *Curr. Clim. Change Rep.*, *1*, 103-113, doi: 10.1007/s40641-015-0007-5.

Kato, S., N. G. Loeb, F. G. Rose, D. R. Doelling, D. A. Rutan, T. E. Caldwell, L. Yu, and R. A. Weller (2013), Surface irradiances consistent with CERES-derived top-of-atmosphere shortwave and longwave irradiances, *J. Clim.*, *26*, 2719–2740, doi:10.1175/JCLI-D-12-00436.1

Khairoutdinov, M. F., and D. A. Randall (2001), A cloud resolving model as a cloud parameterization in the NCAR community climate system model: Preliminary results. *Geophys. Res. Lett.*, *28*, 3617–3620.

Khairoutdinov, M. F., and D. A. Randall (2003), Cloud resolving modeling of the ARM summer 1997 IOP: Model formulation, results, uncertainties, and sensitivities, *J. Atmos. Sci.*, *60*, 607–625.

Kramer, R. J., and B. J. Soden (2016), The sensitivity of the hydrological cycle to internal climate variability versus anthropogenic climate change, *J. Clim.*, *29*, 3661-3673.

Kvalevåg, M. M., B. H. Samset, and G. Myhre (2013), Hydrological sensitivity to greenhouse gases and aerosols in a global climate model, *Geophys. Res. Lett., 40,* 1432–1438, doi:10.1002/grl.50318.

Loeb, N. G., B. A. Wielicki, D. R. Doelling, G. L. Smith, D. F. Keyes, S. Kato, N. Manalo-Smith, and T. Wong (2009), Toward optimal closure of the earth’s top-of-atmosphere radiation budget, *J. Clim., 22,* 748–766.

Lin, J.-L. (2007), The double-ITCZ problem in IPCC AR4 coupled GCMs: Ocean–atmosphere feedback analysis, *J. Climate*, *20*, 4497–4525.

Lu, J., and M. Cai (2009), Stabilization of the atmospheric boundary layer and the muted global hydrological cycle response to global warming, *J. Hydrometeor.*, *10,* 347-352. Doi: 10.1175/2008JHM1058.1.

Mauritsen, T., and B. Stevens (2015), Missing iris effect as a possible cause of muted hydrological change and high climate sensitivity in models, *Nature Geosci.*, *8,* 345-351, doi: 10.1038/ngeo2414.

Mitchell, J. F. B., C. A. Wilson, and W. M. Cunnington (1987), On CO2 climate sensitivity and model dependence of results, *Q. J. Roy. Meteor. Soc.*, *113*, 293-322.

Mlawer, E. J., S. J. Taubman, P. D. Brown, M. J. Iacono, and S. A. Clough (1997), RRTM, a validated correlated-k model for the longwave, *J. Geophys. Res*., *102*, 16663-16682.

Muller, C. J., and P. A. O’Gorman (2011), An energetic perspective on the regional response of precipitation to climate change, *Nat. Clim. Change, 1*, 266–271. doi:10.1038/nclimate1169.

Myhre, G., E. J. Highwood, K. P. Shine, and F. Stordal (1998), New estimates of radiative forcing due to well mixed greenhouse gases, *Geophys. Res. Lett. 25*, 2715-2718. Doi: 10.1029/98GL01908.

Newell, R. E., G. F. Herman, S. Gould-Stewart, and M. Tanaka (1975), Decreased global rainfall during the past Ice Age, *Nature, 253,* 33-34. Doi: 10.1038/253033b0.

O'Gorman, P. A., R. P. Allan, M. P. Byrne, and M. Previdi (2012), Energetic constraints on precipitation under climate change, *Surv. Geophys.*, *33*, 585–608, doi: 10.1007/s10712-011-9159-6.

Ogura T., M. J. Webb, M. Watanabe, F. H. Lambert, Y. Tsushima, and M. Sekiguchi (2014), Importance of instantaneous radiative forcing for rapid tropospheric adjustment, *Clim. Dyn.*, *43*,1409–1421. doi:10.1007/s00382-013-1955-x

Oueslati, B., S. Bony, C. Risi, and J.-L. Dufrense (2016), Interpreting the inter-model spread in regional precipitation projections in the tropics: role of surface evaporation and cloud radiative effects, *Clim. Dyn.*. doi:10.1007/s00382-016-2998-6.

Painemal, D., K.-M. Xu, A. Cheng, P. Minnis, and R. Palikonda (2015), Mean Structure and diurnal cycle of Southeast Atlantic boundary layer clouds: Insights from satellite observations and multiscale modeling framework simulations, *J. Climate, 28,* 324-341. Doi: 10.1175/JCLI-D-14-00368.1.

Previdi, M. (2010), Radiative feedbacks on global precipitation. *Environ. Res. Lett.*, 5, 025211.

Randall, D., M. Khairoutdinov, A. Arakawa, and W. W. Grabowski (2003), Breaking the cloud parameterization deadlock, *Bull. Am. Meteorol. Soc.*, *84*, 1547–1564.

Rayner, N. A., D. E. Parker, E. B. Horton, C. K. Folland, L. V. Alexander, D. P. Rowell, E. C. Kent, and A. Kaplan (2003), Global analyses of sea surface temperature, sea ice, and night marine air temperature since the late nineteenth century, *J. Geophys. Res.*, *108*, 4407, doi:10.1029/2002JD002670.

Richardson, T. B., B. H. Samset, T. Andrews, G. Myhre, and P. M. Forster (2016), An assessment of precipitation adjustment and feedback computation methods, *J. Geophys. Res. Atmos.*, *121*, 11,608-11,619, doi:10.1002/2016JD025625.

Ringer, M. A., T. Andrews, and M. J. Webb (2014), Global-mean radiative feedbacks and forcing in atmosphere-only and coupled atmosphere-ocean climate change experiments, *Geophys. Res. Lett.*, *41*, 4035–4042, doi:10.1002/2014GL060347.

Samset, B. H., et al. (2016), Fast and slow precipitation responses to individual climate forcers: A PDRMIP multimodel study, *Geophys. Res. Lett.*, *43*, 2782–2791, doi:10.1002/2016GL068064.

Stan, C., and L. Xu (2014), Climate simulations and projections with the super-parameterized CCSM4, *Environ. Model. Software*, *60*, 1234-252, doi:10.1016/j.envsoft.2014.06.013.

Stephens, G. L., and T. D. Ellis (2008), Controls of global-mean precipitation increases in global warming GCM experiments, *J. Climate, 21*, 6141-6155. Doi: 10.1175/2008JCLI2144.1.

Stephens, G. L., and Y. Hu (2010), Are climate-related changes to the character of global-mean precipitation predictable? *Environ. Res. Lett.*, *5*, doi:10.1088/1748-9326/5/2/025209.

Vial, J., J.-L. Dufresne, and S. Bony (2013), On the interpretation of inter-model spread in CMIP5 climate sensitivity estimates, *Clim. Dyn.*, *41*, 3339-3362. doi:10.1007/s00382-013—1725.9.

Wang, M., and coauthors (2015), A multi-scale modeling framework model (super-parameterized CAM5) with a higher-order turbulence closure: Model description and low cloud simulations. *J. Adv. Model. Earth Syst.*, *7*, 484-509. doi: 10.1002/2014MS000375.

Wyant, M. C., M. Khairoutdinov, and C. S. Bretherton (2006), Climate sensitivity and cloud response of a GCM with a superparameterization, *Geophys. Res. Lett.*, *33*, L06714, doi:10.1029/2005GL025464.

Wyant, M. C., C. S. Bretherton, P. N. Blossey, and M. Khairoutdinov (2012), Fast cloud adjustment to increasing CO2 in a superparameterized climate model, *J. Adv. Model. Earth Syst.*, *4*, M05001, doi:10.1029/2011MS000092.

Xie, S., H. Ma, J. Boyle, S. Klein, and Y. Zhang (2012), On the correspondence between short- and long-timescale systematic errors in CAM4/CAM5 for the Years of Tropical Convection. *J. Clim. 25*, 7937–7955. doi: 10.1175/JCLI-D-12-00134.1.

Xu, K.-M., and A. Cheng (2013a), Improving low-cloud simulation from an upgraded multiscale modeling framework model, Part I: Sensitivity to spatial resolution and climatology, *J. Climate*, *26*, 5717-5740.

Xu, K.-M., and A. Cheng (2013b), Improving low-cloud simulation from an upgraded multiscale modeling framework model, Part II: Seasonal variations over the eastern Pacific, *J. Climate*, *26*, 5741-5760.

Xu, K.-M., and A. Cheng (2016), Understanding the tropical cloud feedback from an analysis of the circulation and stability regimes simulated from an upgraded multiscale modeling framework. *J. Adv. Model. Earth System, 8*, 10.1002/2016MS000767.

Table 1. Two-year global-averaged surface precipitation rates for SPCAM and SPCAM-IPHOC simulations with 6 and 12 layers below 700 hPa. Unit is mm day^{-1}.

Experiment	SPCAM	SPCAM-IPHOC
6 Layers	2.86	2.88
12 Layers	2.84	2.86

Table 2. Nine-year global-averaged energetic components, and clearsky radiative fluxes and cloud radiative effects at the top of the atmosphere (TOA) and surface, as well as total cloud amount, liquid water path and ice water path for the control runs of SPCAM-IPHOC and SPCAM and their differences. Unit is W m^{-2} for all fluxes. CERES Energy Filled and Balanced (EBAF) radiative fluxes are based upon 16-year (March 2000 to February 2016) averages from the recently updated TOA and surface fluxes (Edition 4.0). The uncertainty estimates of these radiative flux parameters are mostly not available although estimates of upward and downward surface fluxes, not the net fluxes, are available (3-7 W m^{-2}).

	SPCAM-IPHOC	SPCAM	Difference	CERES EBAF
Latent Heating	82.8	83.1	-0.3	
LW Cooling	182.7	181.5	1.2	186.8
SW Absorption	78.8	78.7	0.1	77.1
Surface sensible heat flux	23.4	20.5	2.9	
Residual (H)	-2.4	-0.9	-1.5	
Clearsky LW Cooling	178.2	180.5	-2.3	184.1
Clearsky SW Absorption	73.2	72.4	0.8	72.7
TOA LW cloud radiative effect	22.9	32.5	-9.6	27.9
Surface LW cloud radiative effect	27.2	33.5	-6.3	30.2
TOA SW cloud radiative effect	-50.2	-64.7	14.5	-45.8
Surface SW cloud radiative effect	-55.7	-71.0	15.3	-50.2
Total cloud amount (%)	61.6	57.0	4.6	
Liquid water path (g m^{-2})	98.2	95.5	2.7	
Ice water path (g m^{-2})	48.3	49.5	-1.2	

Table 3. Spatial correlation of precipitation changes with precipitation (P) of the control experiments over the entire tropics and with changes in individual energetic components (SH, H, LWC and SWA) over the tropical lands and ocean. The latter over the entire tropics can be found at the top of panels in Figures 3-6 (b-e).

	SPCAM-IPHOC				SPCAM			
Experiment	2xCO2		+2K		4xCO2		+4K	
P	-0.19		0.49		-0.19		0.56	
	lands	ocean	lands	ocean	lands	ocean	lands	ocean
ΔSH	-0.61	0.27	-0.52	0.30	-0.21	0.14	-0.58	0.28
ΔH	-0.93	-0.99	-0.88	-0.99	-0.81	-0.99	-0.79	-0.99
$\Delta LW_{toa}-LW_{sfc}$	-0.15	-0.54	-0.22	-0.61	-0.28	-0.74	-0.08	-0.60
$\Delta SW_{toa}-SW_{sfc}$	0.63	0.48	0.40	0.20	0.52	0.47	0.38	0.04

Table 4. A few key parameters of the hydrological cycle and sensitivity for SPCAM and SPCAM-IPHOC simulations, in comparison with AMIP5 simulations with and without (*) a slab ocean model and observations (when available) [*Allan et al.*, 2014]. See texts for details.

Parameters	SPCAM	SPCAM-IPHOC	AMIP5	Observations
$\frac{\Delta \boldsymbol{P}}{\boldsymbol{P}}/\Delta T$ (% K^{-1})	3.01	3.57	2.52±0.22	2.83±0.92
LΔP$/\Delta T$ (W m^{-2} K^{-1})	2.50	2.96	2.79±0.26*	n/a
$\Delta R_{ATM}/\Delta T$ (W m^{-2} K^{-1})	2.24	2.47	1.92$\pm$0.16	2.50±0.29
LΔP$/\Delta R_{ATM}$	1.12	1.20	0.83$\pm$0.03	1.09$\pm$0.17
$\Delta(R_{ATM})_{clr}/\Delta T$ (W m^{-2} K^{-1})	2.89	2.98		
LΔP$/\Delta(R_{ATM})_{clr}$	0.87	0.99		
$\Delta P/P$ (%)	6.83	7.90		

*+4K experiment results without a slab ocean model [*Fläschner et al.*, 2016]

Table 5. Global, tropical, tropical land and ocean mean precipitation rate of the control simulations and the changes in precipitation (P), surface sensible heat flux (SH), longwave cooling (LWC), shortwave absorption (SWA), clearsky LWC and SWA, LW and SW cloud radiative effects (CREs) and convergence of dry static energy flux (residual for global mean) between the +SST and control runs. Unit is % except for precipitation. Note that $\Delta P = \Delta LWC - \Delta SWA - \Delta SH - \Delta H$.

	SPCAM				SPCAM-IPHOC			
Parameter	Globe	Tropics	Tropics-Land	Tropics-Ocean	Globe	Tropics	Tropics-Land	Tropics-Ocean
<P> (mm day^{-1})	2.87	3.59	2.44	4.00	2.86	3.67	2.67	4.03
ΔP/<P>	6.83	6.13	-2.79	8.05	7.90	7.00	-0.55	8.77
ΔLWC/<P>	8.20	7.40	10.94	6.64	8.79	8.18	11.53	7.38
ΔSWA/<P>	2.09	2.08	2.60	1.97	2.21	2.21	2.79	2.08
ΔSH/<P>	-0.60	0.06	3.57	-0.70	-0.92	-0.06	2.80	-0.74
ΔH/<P>	-0.12	-0.87	7.56	-2.68	-0.40	-0.97	6.49	-2.73
ΔLWC_{clr}/<P>	10.63	9.97	12.37	9.44	10.65	9.94	12.41	9.36
ΔSWA_{clr}/<P>	2.75	2.69	3.69	2.47	2.72	2.61	3.51	2.39
ΔLWCRE/<P>	2.44	2.57	1.43	2.80	1.86	1.76	0.88	1.98
ΔSWCRE/<P>	-0.66	-0.61	-1.09	-0.50	-0.51	-0.40	-0.72	-0.31

Table 6. Same as Table 5 except for the differences between the xCO2 and control runs.

	SPCAM				SPCAM-IPHOC			
Parameter	Globe	Tropics	Tropics -Land	Tropics-Ocean	Globe	Tropics	Tropics-Land	Tropics-Ocean
$\langle P \rangle$ (mm day^{-1})	2.87	3.59	2.44	4.00	2.86	3.67	2.67	4.03
$\Delta P/\langle P \rangle$	-2.67	-2.80	2.65	-3.97	-2.05	-2.23	5.11	-3.96
$\Delta LWC/\langle P \rangle$	-2.11	-2.15	-4.41	-1.67	-1.99	-2.32	-4.55	-1.25
$\Delta SWA/\langle P \rangle$	0.10	0.05	0.33	-0.01	0.30	0.24	0.76	0.12
$\Delta SH/\langle P \rangle$	0.39	0.51	4.83	-0.42	-0.13	-0.08	0.39	-0.18
$\Delta H/\langle P \rangle$	0.07	0.09	-12.22	2.73	-0.11	-0.25	-10.81	2.77
$\Delta LWC_{clr}/\langle P \rangle$	-1.81	-2.33	-2.54	-2.28	-2.28	-2.52	-2.37	-2.56
$\Delta SWA_{clr}/\langle P \rangle$	0.21	0.15	0.49	0.08	0.30	0.29	0.78	0.17
$\Delta LWCRE/\langle P \rangle$	0.30	-0.18	1.87	-0.61	-0.29	-0.20	2.18	-1.31
$\Delta SWCRE/\langle P \rangle$	-0.11	-0.10	-0.16	-0.09	0.00	-0.05	-0.02	-0.05

Figure captions

Figure 1. Horizontal distributions of surface precipitation rate (multiplied by the latent heat of vaporization) from the control, +2K and 2xCO_2 simulations performed with SPCAM-IPHOC.

Figure 2. Same as Fig. 1 except for the control, +4K and 4xCO_2 simulations performed with SPCAM.

Figure 3. Horizontal distributions of the differences in individual energetic components between the +2K and control experiments performed with SPCAM-IPHOC. The tropical mean and spatial correlation with latent heating are given at the top of each panel (b-e).

Figure 4. As in Figure 3 except for the differences between +4K and control experiments performed with SPCAM.

Figure 5. As in Figure 3 except for the differences between 2xCO_2 and control experiments performed with SPCAM-IPHOC.

Figure 6. As in Figure 3 except for the differences between 4xCO_2 and control experiments performed with SPCAM.

Figure 7. Relative changes of the individual terms in the energetic budget equation: Latent heating (LP), longwave radiative cooling (LWC), shortwave absorption (SWA) and sensible heating over the globe, tropics, tropics-land and tropics-ocean from the SST simulations of SPCAM (SP) and SPCAM-IPHOC (IP).

Figure 8. As in Figure 7 except for the CO2 increase simulations of SPCAM (SP) and SPCAM-IPHOC (IP).

Figure 9. Same as Figure 7 except for the fractional changes of surface evaporation (LH) and the Bowen ratio (LH-SH). The Bowen ratio is defined as SH/LH. Its negative fractional change can be expressed as Δ <LH-SH>/<LH-SH>.

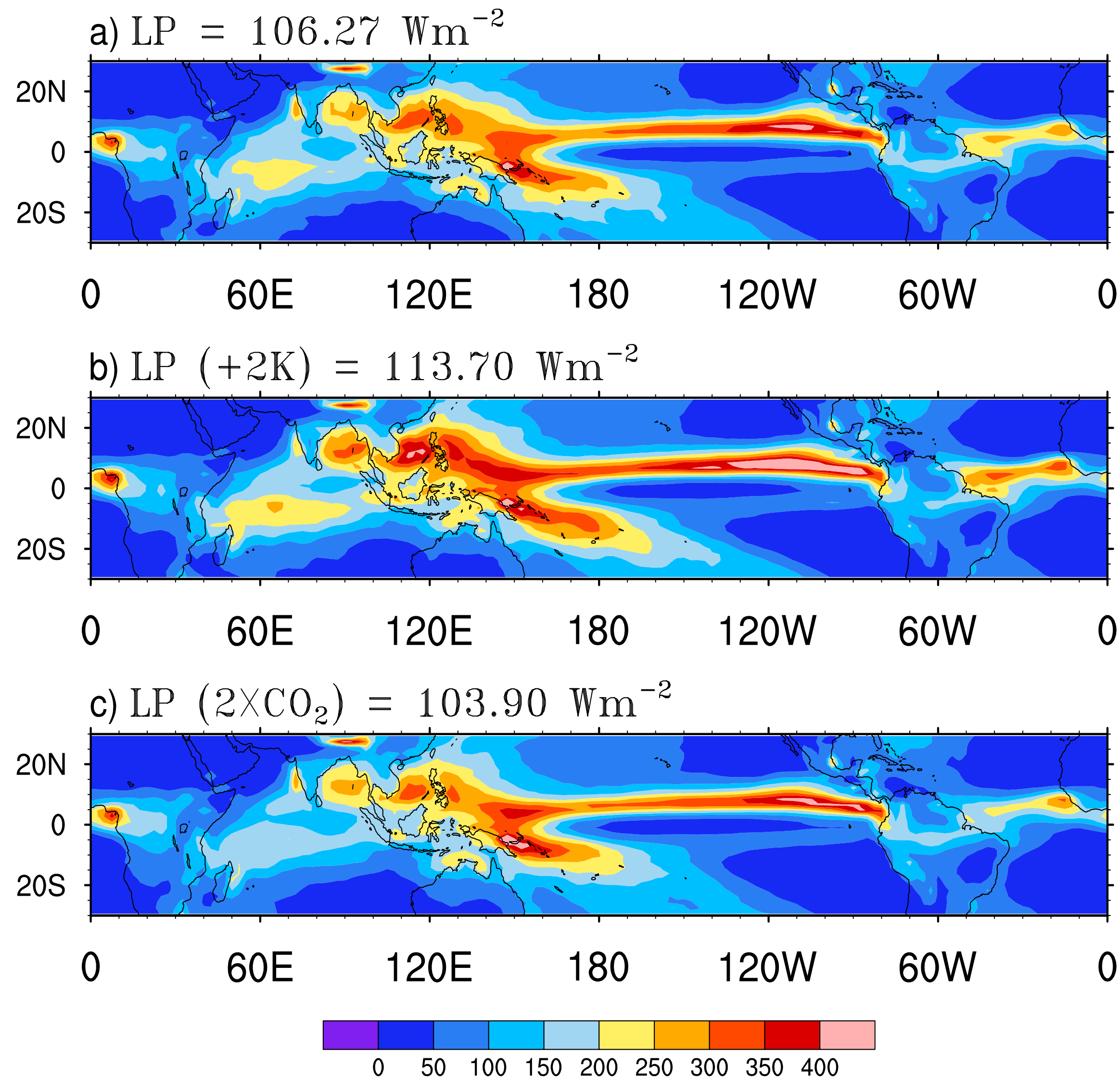

Figure 1. Horizontal distributions of surface precipitation rate (multiplied by the latent heat of vaporization) from the control, +2K and $2xCO_2$ simulations performed with SPCAM-IPHOC.

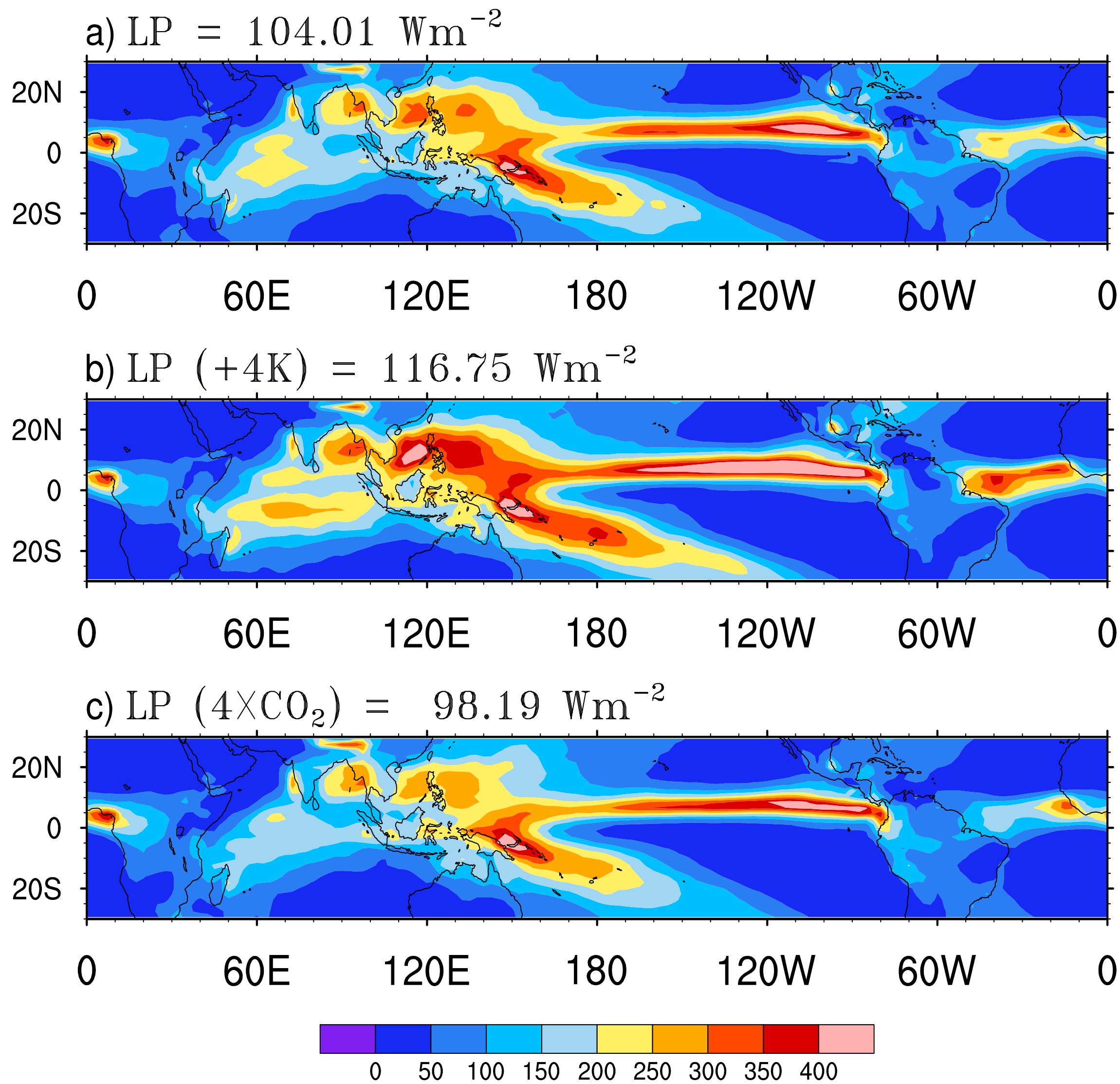

Figure 2. Same as Fig. 1 except for the control, +4K and 4xCO_2 simulations performed with SPCAM.

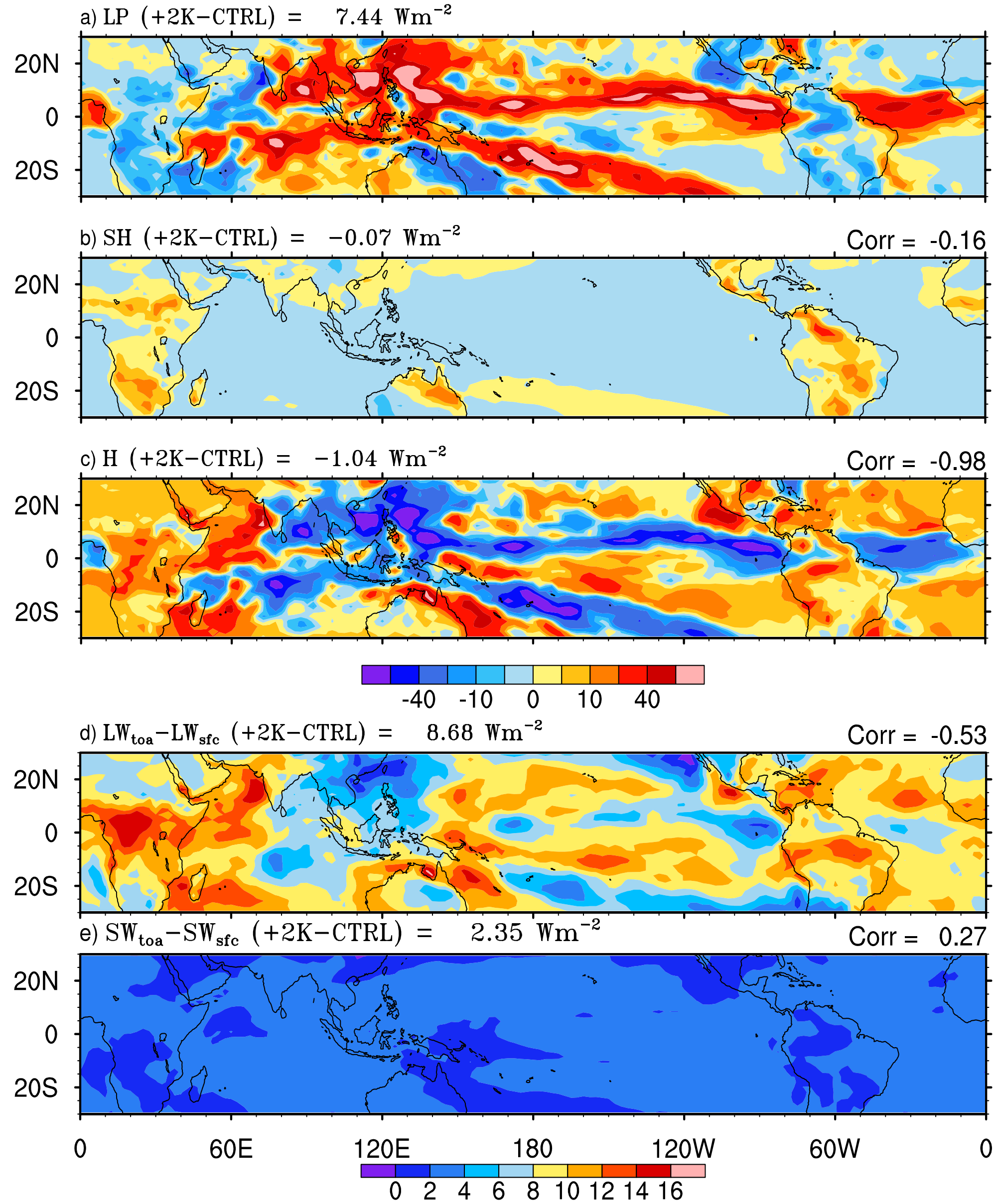

Figure 3. Horizontal distributions of the differences in individual energetic components between the +2K and control experiments performed with SPCAM-IPHOC. The tropical mean and spatial correlation with latent heating are given at the top of each panel (b-e).

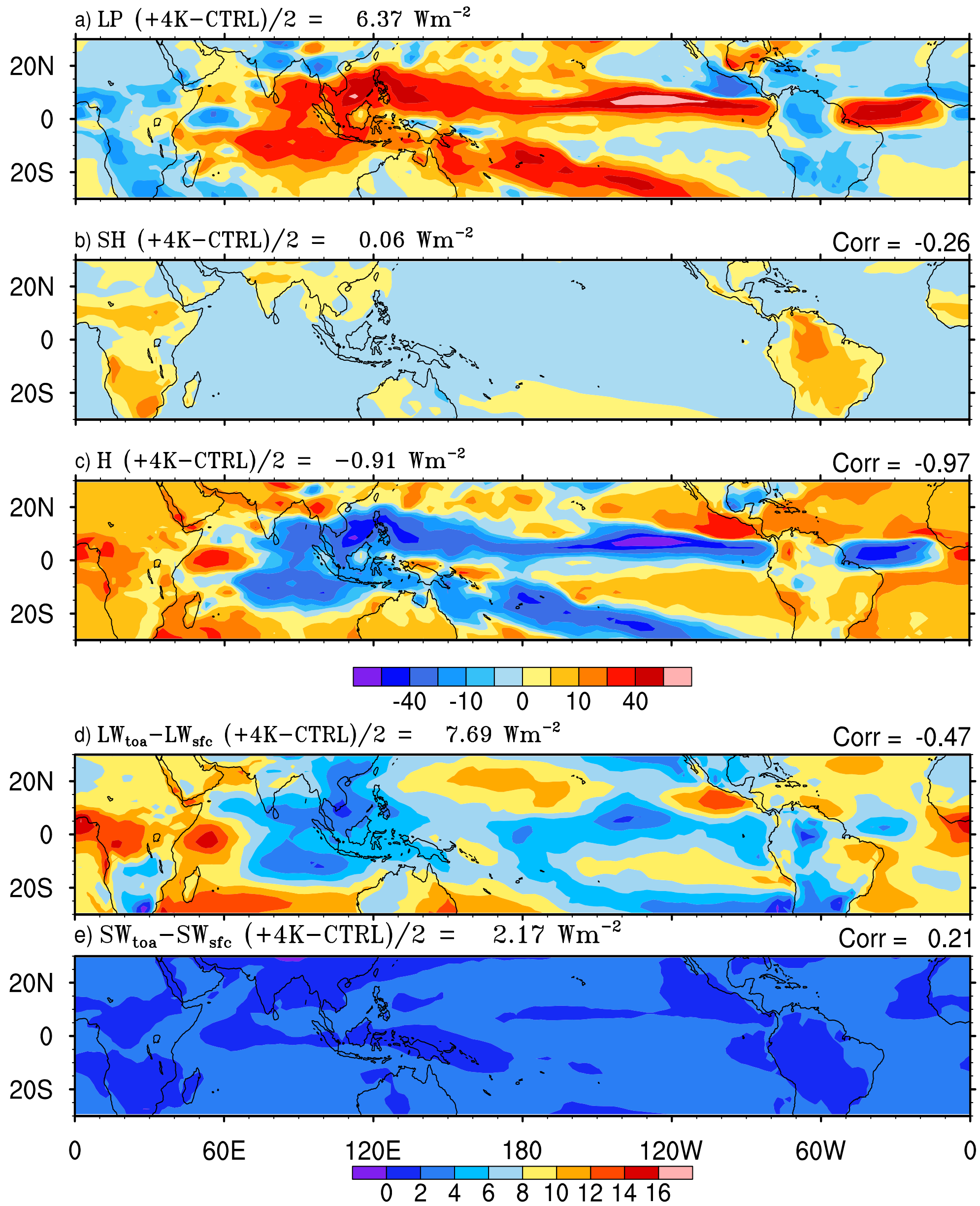

Figure 4. As in Figure 3 except for the differences between +4K and control experiments performed with SPCAM.

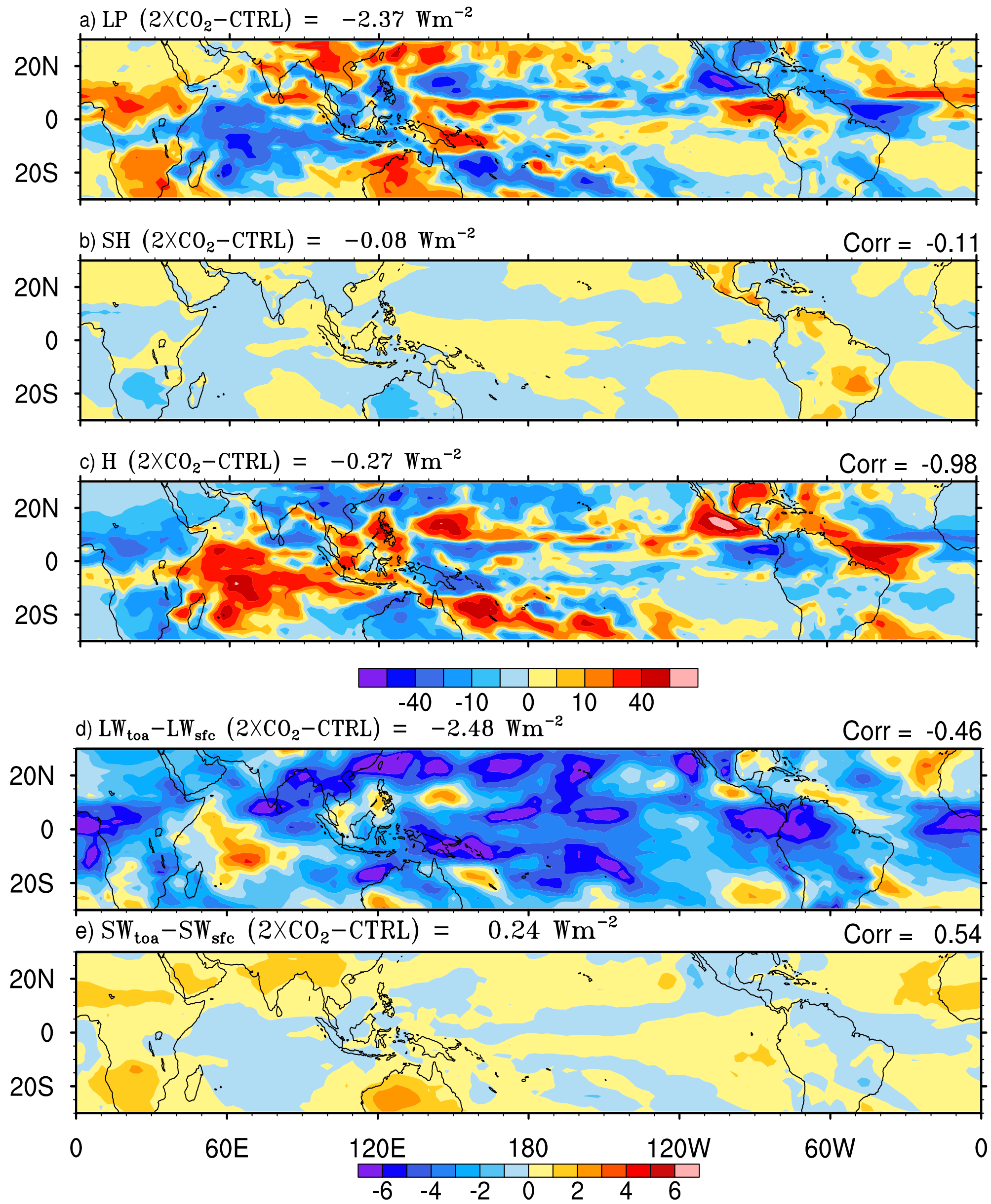

Figure 5. As in Figure 3 except for the differences between 2xCO_2 and control experiments performed with SPCAM-IPHOC.

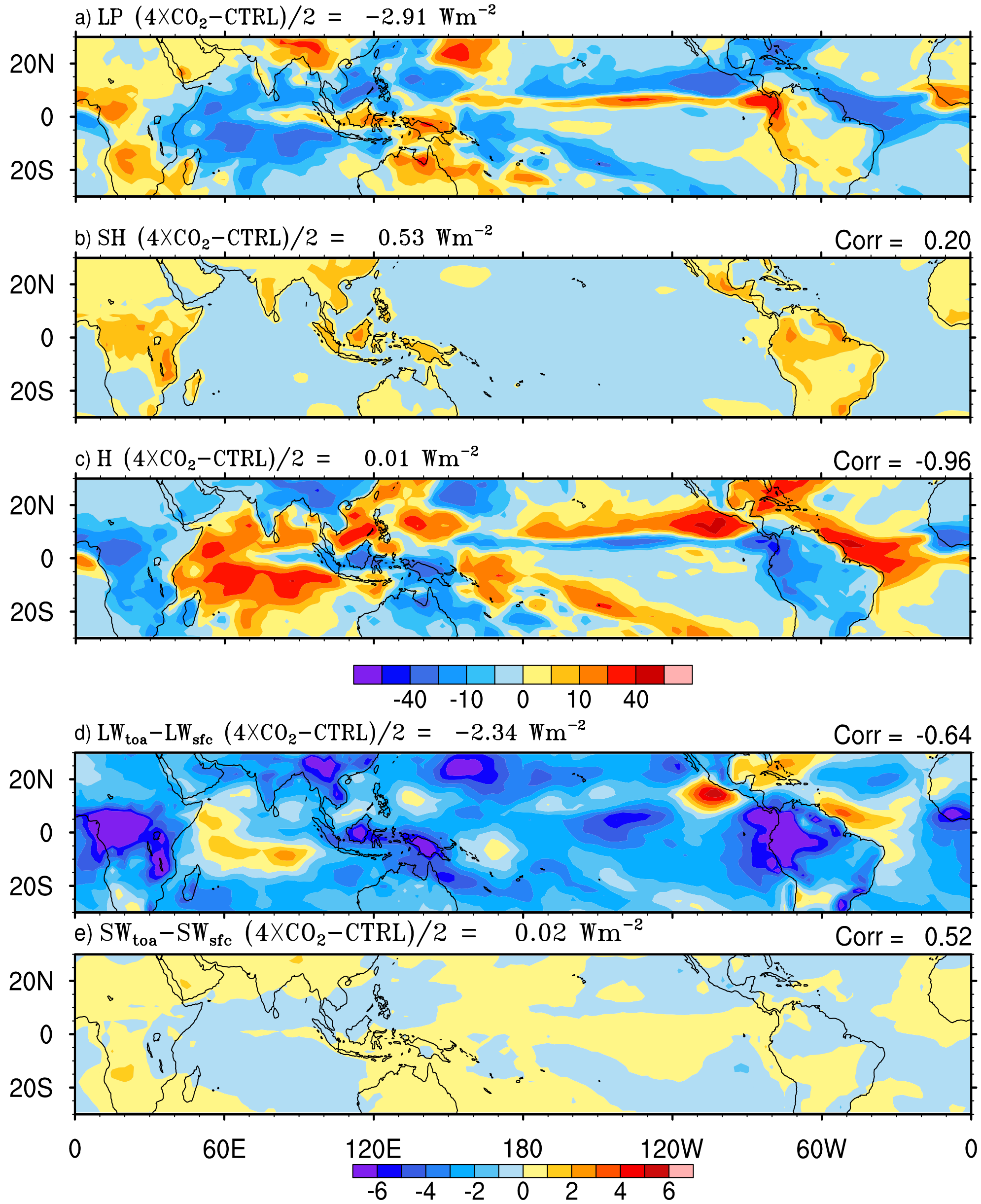

Figure 6. As in Figure 3 except for the differences between 4xCO_2 and control experiments performed with SPCAM.

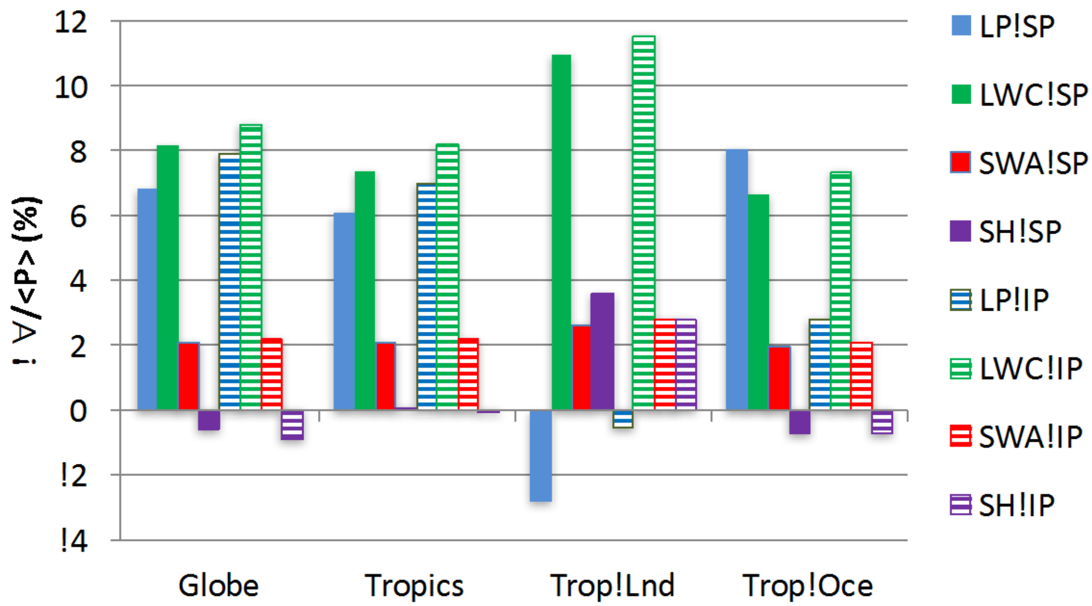

Figure 7. Relative changes of the individual terms in the energetic budget equation: Latent heating (LP), longwave radiative cooling (LWC), shortwave absorption (SWA) and sensible heating over the globe, tropics, tropics-land and tropics-ocean from the SST simulations of SPCAM (SP) and SPCAM-IPHOC (IP).

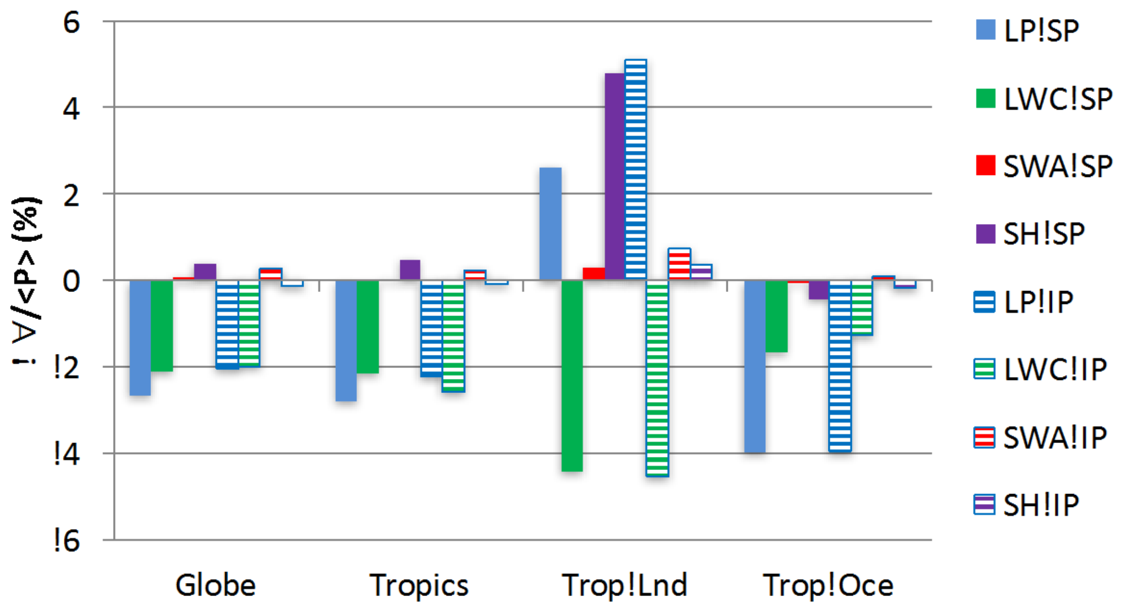

Figure 8. As in Figure 7 except for the CO_2 increase simulations of SPCAM (SP) and SPCAM-IPHOC (IP).

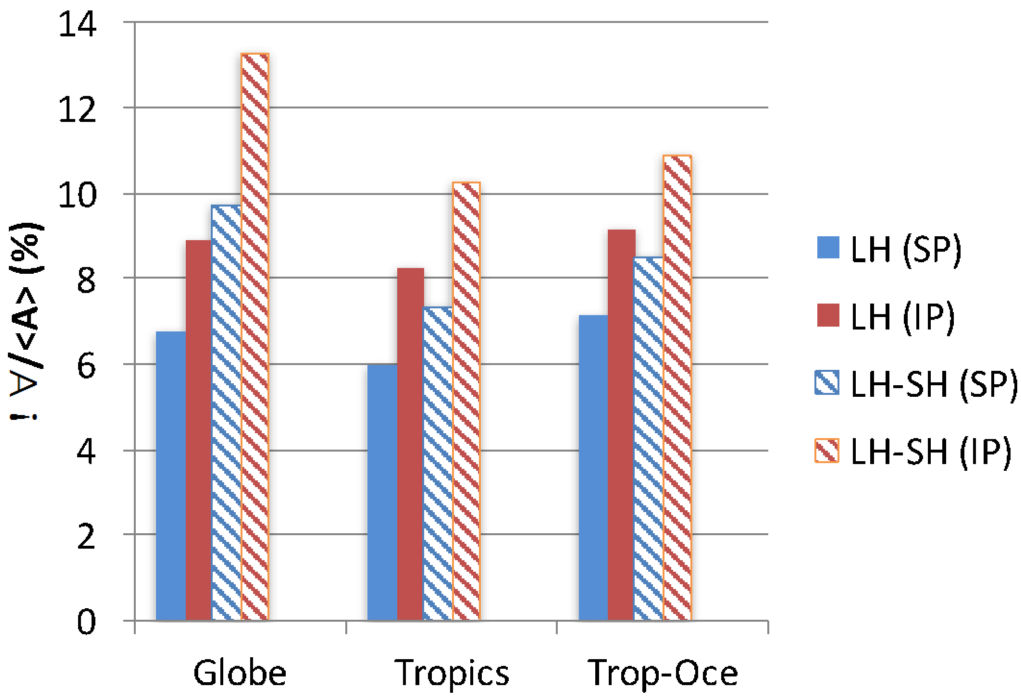

Figure 9. Same as Figure 7 except for the fractional changes of surface evaporation (LH) and the Bowen ratio (LH-SH). The Bowen ratio is defined as SH/LH. Its negative fractional change can be expressed as Δ <LH-SH>/<LH-SH>.